The Electrochemical Society
Advancing solid state & electrochemical science & technology

Insert Zn^{2+} in Tetrahedral Sites of Bi-metal Zn-Co Spinel Oxides with High Oxygen Catalytic Performance for Liquid and Flexible Zinc-Air Batteries

Insert Zn²⁺ in Tetrahedral Sites of Bi-metal Zn-Co Spinel Oxides with High Oxygen Catalytic Performance for Liquid and Flexible Zinc-Air Batteries

Nengneng Xu,[1,2,*] Qi Nie,[1] Jiawen Liu,[3] Haitao Huang,[4] Jinli Qiao,[1,5,z] and Xiao-Dong Zhou[2,**]

[1]*College of Environmental Science and Engineering, Donghua University, Shanghai 201620, People's Republic of China*
[2]*Institute for Materials Research and Innovation, Department of Chemical Engineering, University of Louisiana at Lafayette, Lafayette, Louisiana 70503, United States of America*
[3]*Shanghai Jinyuan Senior High School, Shanghai 200333, People's Republic of China*
[4]*Department of Applied Physics, Hong Kong Polytechnic University, Hong Kong*
[5]*Shanghai Institute of Pollution Control and Ecological Security, Shanghai 200092, People's Republic of China*

Nowadays, it is very challenging to develop a low-cost, highly active and stable bi-functional catalyst for accelerating oxygen reduction reaction (ORR) and oxygen evolution (OER) reaction during the charge and discharge process of zinc-air battery. Herein, we successfully design a novel bi-metal oxide hybrid catalyst ($ZnCo_2O_4$-CNT) by inserting Zn ions. Benefiting from the robust synergetic effects between porous $ZnCo_2O_4$ and CNTs, the high conductivity and the unique nanostructure, the $ZnCo_2O_4$-CNT shows lots of accessible active sites and improved reactants and electrons transfer. As expected, the hybrid shows higher ORR and OER performances with larger limited diffusion current density (5.72 mA cm^{-2}) and lower OER over-potential (0.49 V) than Pt/C and other $ZnCo_2O_4$-CNT samples. In addition, rechargeable zinc-air battery assembled with the bi-functional catalyst exhibits a high power density of 249.4 mW cm^{-2}, a strong discharge durability and charge-discharge stability of 240 cycles. Notably, the flexible zinc-air battery also shows good battery performances with high power density and good flexibility. Hence, exploiting efficient bi-functional catalytic materials with excellent ORR and OER performance and assembling flexible devices will improve the development of current zinc-air batteries battery industry.

Among all kinds of metal-air batteries, zinc-air batteries become a promising candidate for automotive electrification because of the advantages of high power density, low price, high safety factor and environmental friendliness.[1–4] However, the cathode and anode of the zinc-air batteries undergo a sluggish kinetic reaction, namely oxygen reduction (ORR) and oxygen evolution reaction (OER), which involve a complex four-electron transfer pathway and require a strong catalyst for catalysis.[5–8] Nevertheless, the intrinsic activities (ORR and OER) and durability of the bifunctional catalysts are the key to achieve reversible and stable operation of rechargeable zinc-air batteries. To date, one of noble metal catalysts such as Pt/C has excellent ORR properties, but poor OER performance[9,10]; On the other hand, IrO_2 performs well in OER but weak activities for ORR performance.[11,12] Therefore, noble metal catalysts are not ideal candidates to be as bi-functional catalysts, instead, they are expensive. It is serious challenge to develop a low-cost, high-performance bi-functional catalyst for realizing zinc-air batteries large-scale applications.

Co_3O_4 as a classical spinel oxygen electro-catalyst has attracted considerable attention with unique chemical and electronic structure.[13–15] In Co_3O_4 spinel structure, the two types of Co ions can induce different functions.[16,17] In detail, Co^{2+} ion which fills the tetrahedral site serves as the OER active site to form the moieties (-OOH) by the catalytic cycle. While, for ORR, Co^{3+} ion with occupying unit 3d-e_g can offer mediated adsorption ability to the reactive oxygen intermediates owing to the combination of CoO_6 and O_2 on the Co_3O_4 surface. However, in the ordinary structure of Co_3O_4, the overly strong interaction between Co ions and the oxygen intermediates leads to the short bond strength, which further slacken the ORR/OER kinetics. Thus, rationally regulating the characteristic of CoO_6 surface is very important for the development of efficient and durable cobalt-based catalysts.[18] In previous studies, MCo_2O_4 (M = Zn, Fe or Ni) has stronger conductivity and more active sites, showing better ORR/OER performance than pure Co_3O_4.[19,20] Compared with Fe ion and Ni ion, what the replaces Co^{2+} with Zn^{2+} on the tetrahedron in Co_3O_4 does not affect the existence of Co^{3+} on the regular octahedral sites.[21–23] In addition, the doping of Zn^{2+} can further improve the catalytic activity of the catalyst on ORR reaction by optimizing the electron cloud of Co^{3+}.[24] However, improving the conductivity of the kind of catalyst is also formidable challenge. Generally, metal oxides combined with carbon materials (like carbon nanotubes (CNTs) or graphene) can not only improve the conductivity of the composite catalyst, but also increase the specific surface area and improve electrochemical stability.[25–28] Our previous work reported that combining Co_3O_4 with CNTs and N-doping mesoporous carbon (MC) could effectively improve the catalysis of ORR and OER.[29] In addition, $CoFe_2O_4$/N,S-doping graphene oxide (NS-rGO), which is $CoFe_2O_4$ supported on nitrogen/sulfur dual-doped three-dimensional (3D) reduced graphene oxide networks, shows the strong covalent coupling between NS-rGO and $CoFe_2O_4$, endowing the hybrid with a pronounced ORR and OER activity and stability (comparable to that of the precious metal catalyst).[26] Inspired by this, the conductivity of the $ZnCo_2O_4$ catalyst can be further improved by adding carbon material, which endows the composite excellent electrochemical activity.

Based on the design strategy, we herein synthesize a bi-functional $ZnCo_2O_4$-CNT composite catalyst through a one-step hydrothermal method. Interestingly, the CNT of the hybrid offers a quick electron transfer pathway, and the porous structure of the material provides rich reactive areas. Electrochemical tests demonstrate that the $ZnCo_2O_4$-CNT have a superior ORR/OER activity (positive half-potential: 0.76 V and low OER potential: 0.49 V) and long-term durability than Pt/C, which is attributed to its strong

*Electrochemical Society Student Member.
**Electrochemical Society Member.
zE-mail: qiaojl@dhu.edu.cn

synergistic interaction between two components and the accurate regulation of electron structure by inserting Zn ions. The primary and rechargeable zinc-air battery exhibits remarkable power density (249.4 mW cm^{-2}), small discharge-charge polarization (1.43 V at 65 mA cm^{-2}) and good stability (240 cycles). Finally, we applied the catalyst to flexible zinc-air batteries and bent batteries at different angles (0°, 30° and 150°), demonstrating decent battery performance and flexibility. This work should shed light on developing high performance bifunctional catalyst by the conception of Zn^{2+} insertion.

Experimental

Synthesis of catalyst.—The synthesis description of ZnCo$_2$O$_4$-CNT can be reflected in Fig. 1. Firstly, 0.2 g of Co (AC)$_2$ 2H$_2$O and 0.2 g of Zn (AC)$_2$ 2H$_2$O are dissolved in 15 ml of aqueous ammonia, and stirring until the solid particles are completely dissolved. Subsequently, 0.05 g of carbon materials (Carbon Nanotubes: CNTs, Graphene and Porous Carbon: MC) were added for parallel tests, respectively. After magnetic stirring for more than 4 h, three kinds of uniformly dispersed solutions were obtained. Then, the solutions were transferred to autoclaves with the volume of 50 ml and placed them into ovens to start the hydrothermal reaction, the temperature and time were set to 140 °C and 6 h, respectively. After the reaction completed, the obtained products were centrifugally washed several times with deionized water and absolute ethanol until they became neutral. Finally, calcination was carried out at 350 °C for 1 h with the heating rate of 3 °C min^{-1}. The calcined black particles were ground into fine powders and named as

ZnCo$_2$O$_4$-CNT, ZnCo$_2$O$_4$-graphene and ZnCo$_2$O$_4$-MC. In order to investigate the effect of the Zn ions doping on the electrochemical properties of the catalytic materials, the catalyst with the carbon materials (CNTs) was added at a Co ions solution without Zn ions. The obtained catalysts could be named as Co$_3$O$_4$-CNT. In addition, in order to explore the best heating temperature and time of the catalytic material, the catalysts with the optimal carbon material (CNTs) and the optimal Co-Zn metal ratio (1:1) were used and heated at 120, 140, 160 and 180 °C for 6 h to investigate the effect of different hydrothermal temperatures. On the other hand, these catalysts were also heated at 140 °C for 4 h, 6 h, 8 h and 10 h to investigate the effect of different hydrothermal time. Finally, these products were calcined in air at 350 °C for 1 h, the obtained catalysts can be named as ZnCo$_2$O$_4$-CNT-120, ZnCo$_2$O$_4$-CNT-140, ZnCo$_2$O$_4$-CNT-160, ZnCo$_2$O$_4$-CNT-180 and ZnCo$_2$O$_4$-CNT-4, ZnCo$_2$O$_4$-CNT-6, ZnCo$_2$O$_4$-CNT-8, ZnCo$_2$O$_4$-CNT-10.

Material characterization.—Scanning electron microscopy (SEM) image was obtained by JSM-5600 lV microscope at an accelerating voltage of 15 kV. Transmission electron microscopy (TEM), high-resolution transmission electron microscopy (HRTEM) and mapping images were obtained by JEM-2100F microscope at an accelerating voltage of 200 kV. X-ray diffraction (XRD) image was obtained by D/MAX-2550 PC X-ray diffractometer using a Cu Kα radiation of 0.15405 nm, a current of 40 mA, a voltage of 30 kV and the scan angle 2θ is in the range of 5°–90°. X-ray photoelectron spectroscopy (XPS) images were obtained by RBD-upgraded PHIe 5000 C ECSA system using an Al Kα X-ray radiation anode source
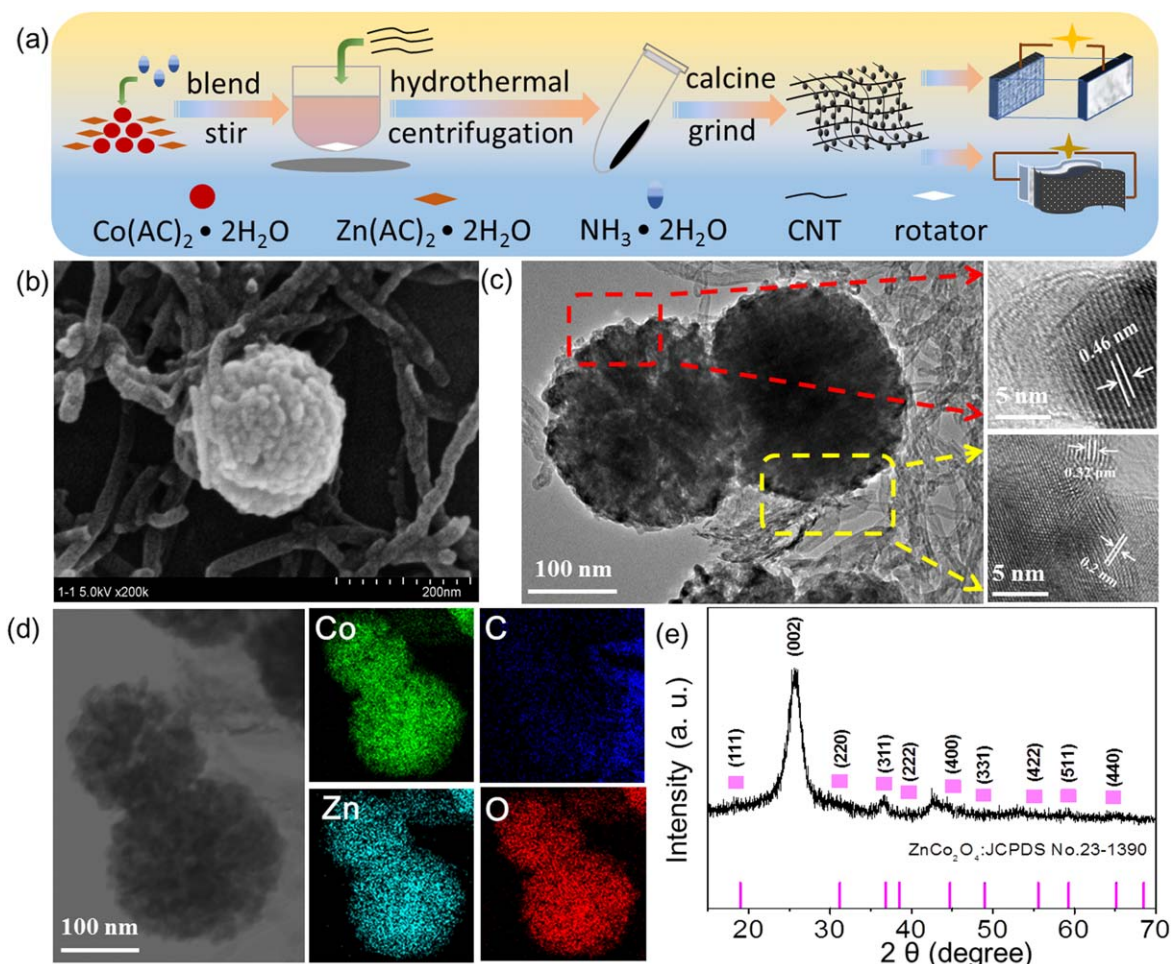

Figure 1. (a) Illustration of the synthesis procedure of ZnCo$_2$O$_4$-CNT-140/6 catalyst; (b) SEM image of ZnCo$_2$O$_4$-CNT-140/6 catalyst; (c) TEM and HRTEM images of ZnCo$_2$O$_4$-CNT-140/6 catalyst; (d) Mapping images of ZnCo$_2$O$_4$-CNT-140/6 catalyst; (e) The XRD pattern of ZnCo$_2$O$_4$-CNT-140/6 catalyst.

of 1484.6 eV, an accelerating voltage of 14000 V and a capacity of 250 W.

Electrochemical tests.—It is operated at normal temperature and pressure through a CHI 760D electrochemical station system in a conventional three-electrode cell reactor (150 ml capacity). The three-electrode cell includes counter electrode (Pt rod), working electrode (rotating disc electrode (RDE, dm = 5 mm)) and reference electrode (saturated calomel electrode (SCE)). The working electrode is prepared by the following steps. Firstly, 2 mg catalyst was dissolved in 1 ml of ethanol and 8 μl of Nafion solution (5 wt%). The catalyst ink was ultrasonically dispersed for half an hour and then taken out for use. Then, 24 μl of the catalyst solution was pipetted into the clean glassy carbon electrode, then allowing it to dry naturally, so that the catalyst loading on the glassy carbon electrode is 0.24 mg cm^{-2}. Finally, the three electrodes are placed together in the reactor and clamped with electrode clips. 0.1 M KOH solution is poured into the cell reactor. After the oxygen is introduced into the solution for half an hour, the electrochemical tests could be started. All the measured potential data needs to be converted into a reversible hydrogen electrode (RHE) data before it can be used (E (vs RHE) = E (vs SCE) + 0.9934 V). The voltage window of ORR test is from 0.2 to 1.1 V at a scan rate of 5 mV s^{-1} at 300, 600, 900, 1200, and 1500 rpm different electrode rotating speeds. The voltage window of OER tests are from 1 to 2 V at 1500 rpm electrode rotating speed.

Air electrode preparation.—In a traditional liquid zinc-air battery, a carbon paper with the area of 16 cm^2 with the model of Toray TGP-H-030 was prepared and sonicated for 30 min for two times. Dip the carbon paper completely into polytetrafluoroethylene (PTFE, 30 wt%) solution for 30 s and dried at 60 °C. Then the carbon paper with the bake-dry diffusion layer was calcined in air at 350 °C for 1 h with the heating rate of 3 °C min^{-1}. At the same time, the catalyst ink was made up of 30 mg of the catalyst, 10 mL of ethanol and 80 μl of Nafion solution (5 wt%). Spraying the catalyst ink onto the middle of the carbon paper with the loading of about 2 mg cm^{-2} and the area of 1 cm^2.

In a flexible zinc-air battery, carbon cloth with the area of 4 cm^2 with the model of WOS1002 was prepared, the catalyst ink is configured using the above method. Spraying the catalyst ink onto the carbon cloths with the loading of about 2 mg cm^{-2} and the area of 3 cm^2.

The fabrication and measurements of zinc-air batteries.—A traditional liquid zinc-air battery includes air electrode as cathode (the carbon paper, 16 cm^2 in area) with bifunctional catalyst (1 cm^2 in area), zinc plate (over 99.99% in purity and 0.5 mm in thickness, Shengshida Metal Mater. Co. Ltd., China) as anode and 6 M KOH as electrolyte. A flexible zinc-air battery includes a cathode air electrode (the carbon cloths, 4 cm^2 in area) with catalyst (3 cm^2 in area), an anode zinc foil (over 99.99% in purity and 0.01 mm in thickness, Shengshida Metal Mater. Co. Ltd., China) and the Tokuyama A 201 electrolyte membrane (3 cm^2 in area, 11.4 mS cm^{-1} in OH$^-$ conductivity and 1.7 meq g^{-1} in ion-exchange capacity). It is worth noting that a series of treatments are required before the dry film is used. The membrane was first placed in a 2 M KOH solution and allowed to stand for 30 min. At time, it was taken out, rinsed with deionized water, and allowed to stand in deionized water for 30 min. After the above process is repeated, the film treatment is completed. The zinc foil, the treated Tokuyama A 201 membrane, and the catalyst-coated carbon cloth were stacked in this order. Next, a small amount of alkaline binder was used to bond each of them. Finally, followed by a hot press, making the three-layer material become a whole battery. The hot pressing was operated under the temperature of 50 °C, the time of 5 min, and the pressure of 3 Mpa. A galvanodynamic method was used to measure the maximum power density, the discharge time and the stability of charge and discharge tests.

Results and Discussion

The morphology and microstructure of ZnCo$_2$O$_4$-CNT-140/6 catalyst was observed by SEM. The ZnCo$_2$O$_4$ shows a flower-shaped microsphere-like 3D configuration (Fig. 1b). The diameter of the ZnCo$_2$O$_4$ is approximately 250 nm and is dispersed around CNTs. ZnCo$_2$O$_4$ spheres are composed of different micro-sized particles. The sizes of small particles are about 6.4–28.1 nm. The condensation of small particles makes the sphere appear rough surface and porous interior, further increasing the specific surface area of ZnCo$_2$O$_4$-CNT-140/6 catalyst. In addition, the rough surface and porous interior maybe improve electrolyte permeation and adjust accommodate volume changes during charge-discharge cycles. In order to explore the physical properties of ZnCo$_2$O$_4$-CNT-140/6 catalyst deeply, TEM and HR-TEM were carried out. As shown in Fig. 1c, ZnCo$_2$O$_4$ particles are spirally wound around the surrounding CNTs. The sizes of the two ZnCo$_2$O$_4$ particles are about 270.5–284.2 nm, and the ZnCo$_2$O$_4$ particles shows 3D balls-like morphology. The ball is also filled with small and uneven particles, corresponding to the SEM result. Moreover, HR-TEM is further observed that a lattice spacing of the ZnCo$_2$O$_4$-CNT-140/6 catalyst is 0.46 nm, which should be correspond to (111) plane. The lattice spacing of 0.32 nm and 0.2 nm correspond to the (220) and (311) planes of ZnCo$_2$O$_4$ particles, respectively. Moreover, the distribution of Co, Zn, C and O elements were evenly distributed on ZnCo$_2$O$_4$ particles, which demonstrates the successful synthesis of the binary metal oxide composite catalyst (Fig. 1d). In order to investigate the microscopic material composition inside the catalytic material, XRD pattern was carried out to study the crystal structure. Figure 1e shows the XRD curve of ZnCo$_2$O$_4$-CNT-140/6 catalyst, which corresponding to spinel-phase ZnCo$_2$O$_4$ (JCPDS No. 23-1390). Due to the presence of CNTs, the carbon peak with a crystal plane of 002 occurring at 2θ of 25.48 is higher, which weakens the peak height of ZnCo$_2$O$_4$. It is not difficult to find that almost all the peaks on the ZnCo$_2$O$_4$-CNT-140/6 curve have corresponding crystal faces, which further proves the successful synthetization of the binary metal composite oxide ZnCo$_2$O$_4$.[30]

In order to explore the changes of surface chemical composition and binding energy of ZnCo$_2$O$_4$-CNT-140/6 catalyst, the XPS spectra of Zn 2p, Co 2p and O 1 s were analyzed (Fig. 2a). As shown in Fig. 2b, one peak of Zn 2p at 1021.7 eV is Zn 2p$_{3/2}$ level, and the other peak at 1044.9 eV is attributed to Zn 2p$_{1/2}$ level, demonstrating the presence of the Zn^{2+}.[31] In Fig. 2c, the diffraction peaks at 780.6 eV and 795.6 eV are corresponded to Co 2p$_{3/2}$ and Co 2p$_{1/2}$ levels,[32] respectively. The 15 eV gap between the two peaks is consistent with the literature.[33,34] There are two weak satellite peaks at 790.1 eV and 805.1 eV, and the energy gap between the main peak and the satellite peak is 9.7 eV, revealing the existence of Co^{3+}.[35–37] Co^{3+} have been known to be ORR active site. In Fig. 2d, O 1 s can be attributed to the oxygen from OH$^-$ at the 531.7 eV diffraction peak and the oxygen generated by a small amount of physically adsorbed water molecules at the 533.5 eV diffraction peak.[38–41] Based on these results, Zn^{2+} successfully replaces the tetrahedral field Co^{2+}, which increase the Co-O bond length by forming Zn-O-Co substitution.[18,42,43] The change of the bond will improve the ORR and OER catalytic activity of ZnCo$_2$O$_4$-CNT-140/6.

As a good conductive material, different carbons will have different effect on ORR/OER activity of ZnCo$_2$O$_4$ due to their unique structure. Figure 3a shows the ORR curves of ZnCo$_2$O$_4$ with different carbon materials. Compared to ZnCo$_2$O$_4$-Graphene and ZnCo$_2$O$_4$-MC, ZnCo$_2$O$_4$-CNT-140/6 shows a more positive onset potential (j = 0.1 mA cm^{-2}) of catalyst of 0.97 V and the half-wave potential of 0.76 V. Moreover, the limited diffusion current density of 5.72 mA cm^{-2} is higher than ZnCo$_2$O$_4$-Graphene (4.49 mA cm^{-2}) and ZnCo$_2$O$_4$-MC (4.24 mA cm^{-2}) catalyst. For OER, ZnCo$_2$O$_4$-CNT-140/6 also shows higher OER activity with a low potential of 1.72 V at 10 mA cm^{-2} and a large current density of 38.52 mA cm^{-2} at 2.0 V than ZnCo$_2$O$_4$-Graphene (1.77 V and 28.55 mA cm^{-2}) and ZnCo$_2$O$_4$-MC (1.77 V and 26.17 mA cm^{-2}).
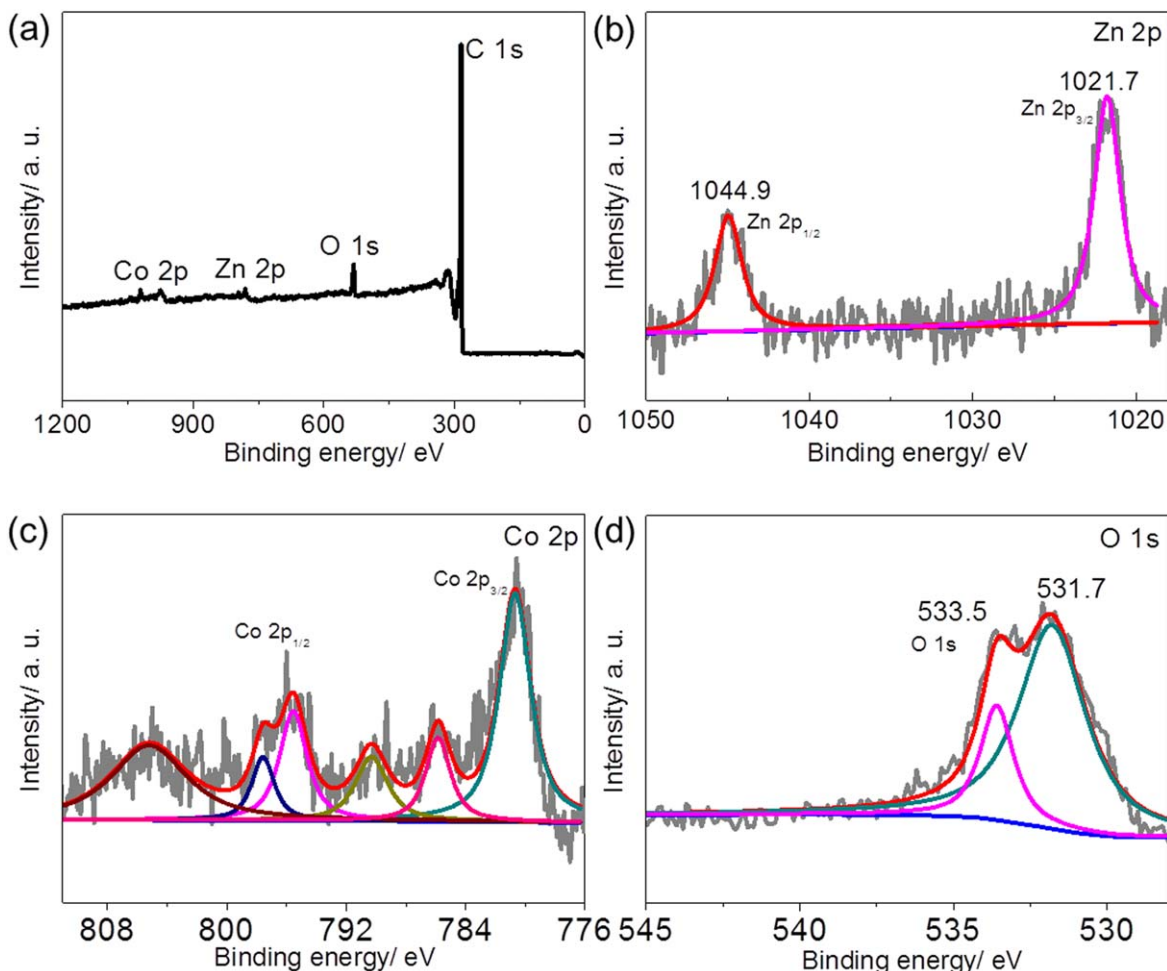
Figure 2. XPS spectrum of $ZnCo_2O_4$-CNT-140/6 catalyst of (a) Overall spectrum; High-resolution curves of (b) Zn 2p region, (c) Co 2p region, (d) O 1 s region.

The result reveals, compared to graphene and MC, CNTs can better improve the ORR and OER activity of $ZnCo_2O_4$ due to its unique structure and the unique effect between $ZnCo_2O_4$ and CNT. In addition, $ZnCo_2O_4$-CNT-140/6 shows improved ORR activity compared with bi-metal $ZnCo_2O_4$, CNT and Co_3O_4/CNT, which is although slightly lower than the commercial Pt/C. For OER, $ZnCo_2O_4$-CNT-140/6 exhibits the best OER activity than $ZnCo_2O_4$, CNT, Co_3O_4/CNT and Pt/C. These results further indicate that i) the strong synergy between $ZnCo_2O_4$ and CNT; ii) Zn^{2+} ions insertion greatly accelerated the catalyst activity; iii) CNTs has large specific surface area and excellent electrical conductivity, facilitating the electron transfer. In addition, $ZnCo_2O_4$ is composed of many fine nanoparticles and shows the unique prous morphology, which also create abundant buffer zones and provide more active sites. This result is also consistent with SEM and TEM results. Figures 3c and 3d shows the electron transfer number of $ZnCo_2O_4$-CNT-140/6 catalyst is 3.89, which is close to the commercial precious metal Pt/C with electron transfer number of 3.98 (Figs. 3e and 3f), revealing that the ORR proceeds of the bi-metal oxide catalyst via a 4e-transfer pathway.

In addition, the $ZnCo_2O_4$-CNT-140/6 not only has a high activity, but also has a strong durability of ORR and OER in 0.1 M KOH solution. To evaluate the electrochemical stability of $ZnCo_2O_4$-CNT-140/6 catalyst, the stability tests were implemented by using RDE with the scan rate of 5 mV s^{-1} after 2000 cycles CVs. The results of $ZnCo_2O_4$-CNT-140/6 catalyst stability after scanning are shown in Fig. 4. Compared with the initial curve, for ORR, the onset potential of the hybrid is only attenuated 0.13 V, the limiting current density is only reduced by 0.72 mA cm^{-2} (Fig. 4a).

Similarly, for OER, the current density at 2 V after stability testing is 32.05 mA cm^{-2}. The corresponding potential at 10 mA cm^{-2} is 1.77 V. Compared with the previous OER curve, the current density at 2 V is only attenuated 6.47 mA cm^{-2}, and the over-potential difference is only 0.05 V. All of the above data indicates the $ZnCo_2O_4$-CNT-140/6 catalyst has excellent oxygen reduction and oxygen evolution stability.

In order to explore the optimal hydrothermal temperature and time, the samples of different hydrothermal temperatures (120, 140, 160 and 180 ^{o}C) and different hydrothermal time (4, 6, 8 and 10 h) are measured. Figures 5a and 5b show the ORR and OER curves of $ZnCo_2O_4$-CNT catalyst at different hydrothermal temperatures (120, 140, 160 and 180 ^{o}C) for same hydrothermal time (6 h). The results show that $ZnCo_2O_4$-CNT-140 catalyst has the most efficient ORR and OER performance when the hydrothermal temperature is 140 ^{o}C.

Figures 5c and 5d show the ORR and OER performance of $ZnCo_2O_4$-CNT catalyst at 140 ^{o}C for different hydrothermal time (4, 6, 8 and 10 h). $ZnCo_2O_4$-CNT-6 catalyst has the most efficient ORR and OER performance among all samples. Above all, $ZnCo_2O_4$-CNT obtained at 140 ^{o}C for 6 h exhibits the excellent electrochemical performance, which should be attributed to the formation of unique morphology and structure.

In order to evaluate the practicability of the $ZnCo_2O_4$-CNT-140/6 catalyst, a zinc-air battery was assembled using these catalyst samples. For all battery test, the catalyst loading on carbon paper was 2 mg cm^{-2}. As shown in Fig. 6a, the open circuit voltages of $ZnCo_2O_4$-CNT-140/6 and commercial Pt/C catalysts are 1.44 and 1.46 V under air operation conditions, respectively. The current density of $ZnCo_2O_4$-CNT-140/6 catalyst is large to 698.3 mA cm^{-2},
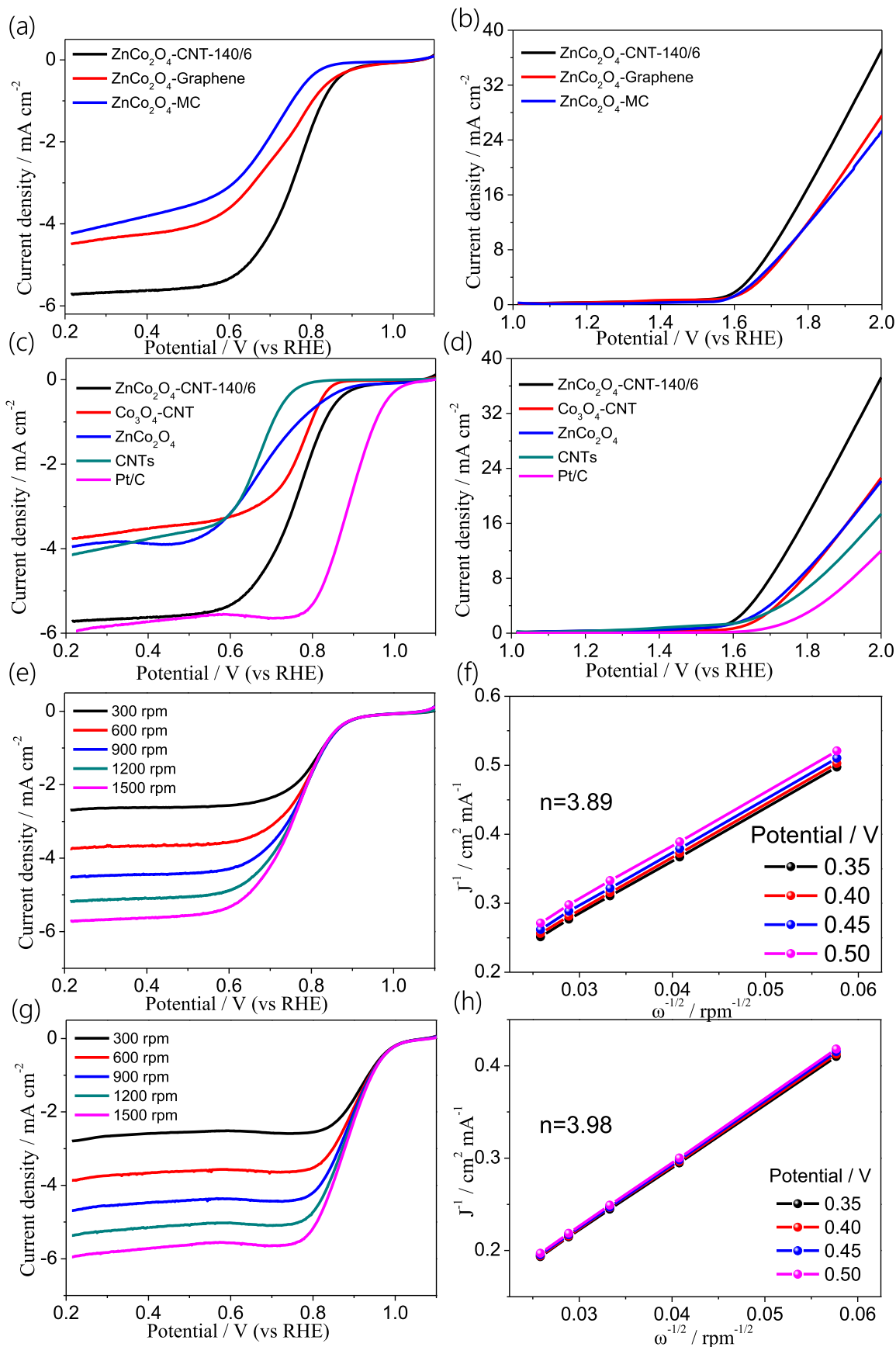
Figure 3. (a) ORR polarization curves and (b) OER polarization curves of ZnCo$_2$O$_4$-CNT-140/6, ZnCo$_2$O$_4$-Graphene and ZnCo$_2$O$_4$-MCcatalysts; (c) polarization curves and (d) OER polarization curves of ZnCo$_2$O$_4$-CNT-140/6, Co$_3$O$_4$-CNT, ZnCo$_2$O$_4$, CNTs and Pt/C catalysts; (e) the ORR curves of ZnCo$_2$O$_4$-CNT-140/6 at various rotation rates; (f) the K-L plots and the number of electrons transferred of of ZnCo$_2$O$_4$-CNT-140/6; (g) the ORR curves of Pt/C at various rotation rates; (h) the K-L plots and the number of electrons transferred of Pt/C.
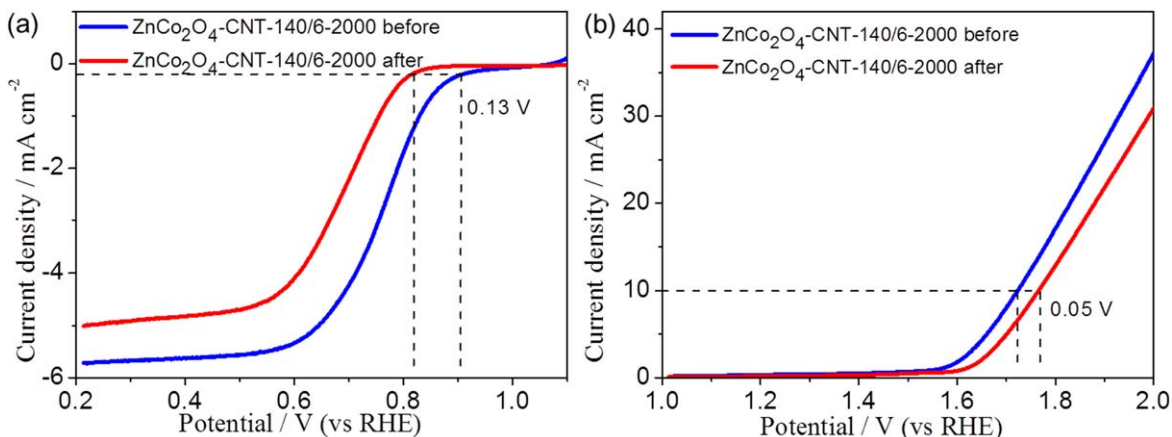
Figure 4. (a) ORR polarization curves of the cycle stability of $ZnCo_2O_4$-CNT-140/6 catalyst; (b) OER polarization curves of the cycle stability of $ZnCo_2O_4$-CNT-140/6 catalyst.

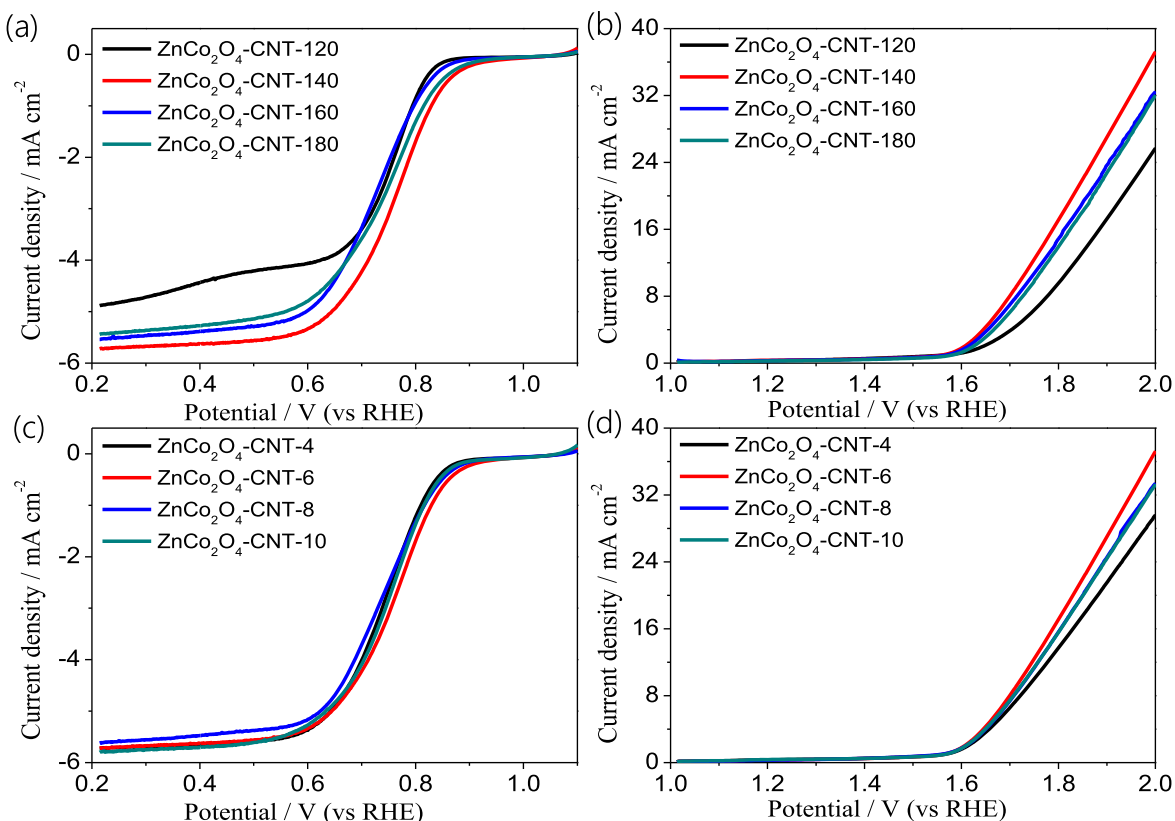**Figure 5.** ORR and OER polarization curves of $ZnCo_2O_4$-CNT catalyst of (a)–(b) different hydrothermal temperatures; (c)–(d) different hydrothermal time.

which is twice that of Pt/C catalysts (336.3 mA cm^{-2}). In addition, $ZnCo_2O_4$-CNT-140/6 catalyst have a highest power density of 249.4 mW cm^{-2} among all composed catalysts (Figs. S1a and S1b is available online at stacks.iop.org/JES/167/050512/mmedia), which even exceeds Pt/C catalysts (221.2 mW cm^{-2}). In order to further prove the primary battery performance, the discharge cycle at different current density were carried out. In detail, the current density started from 5 mA cm^{-2}, incrementing by 5 mA cm^{-2} every 30 min, until the current density increasing to 50 mA cm^{-2} and then again from 5 mA cm^{-2} to begin a cyclic gradual current discharge. As shown in Fig. 6b, the commercial Pt/C catalyst exhausted after only 2.8 h, while $ZnCo_2O_4$-CNT-140/6 catalyst still discharging. Moreover, the discharge time of $ZnCo_2O_4$-CNT-140/6 catalyst can reach 17.97 h (working voltage > 1 V) at the discharge cycle with different current density of 5–50 mA cm^{-2}. These results further

prove that the successful application of $ZnCo_2O_4$-CNT-140/6 catalyst in primary batteries, also demonstrate the ideal stability of $ZnCo_2O_4$-CNT-140/6 catalyst. It is consistent with the durability and activity of the ORR/OER test in Figs. 3 and 4. For long-term discharge, the primary zinc-air battery of $ZnCo_2O_4$-CNT-140/6 catalyst discharges over 51.57 h with a high coulomb efficiency of 91.8% at a high current density of 30 mA cm^{-2}, which is about 13 h longer than the noble metal catalyst (Pt/C: 38.82 h, 85.5%). In a word, $ZnCo_2O_4$-CNT-140/6 catalyst have a good potential in primary zinc-air battery applications. Besides the primary zinc-air battery, the charge and discharge performance of $ZnCo_2O_4$-CNT-140/6 catalyst is tested in a home-made rechargeable zinc-air battery. Figure 6d shows the charge-discharge polarization curves of $ZnCo_2O_4$-CNT-140/6 and Pt/C. As the current density increases, the charge-discharge voltage difference between the
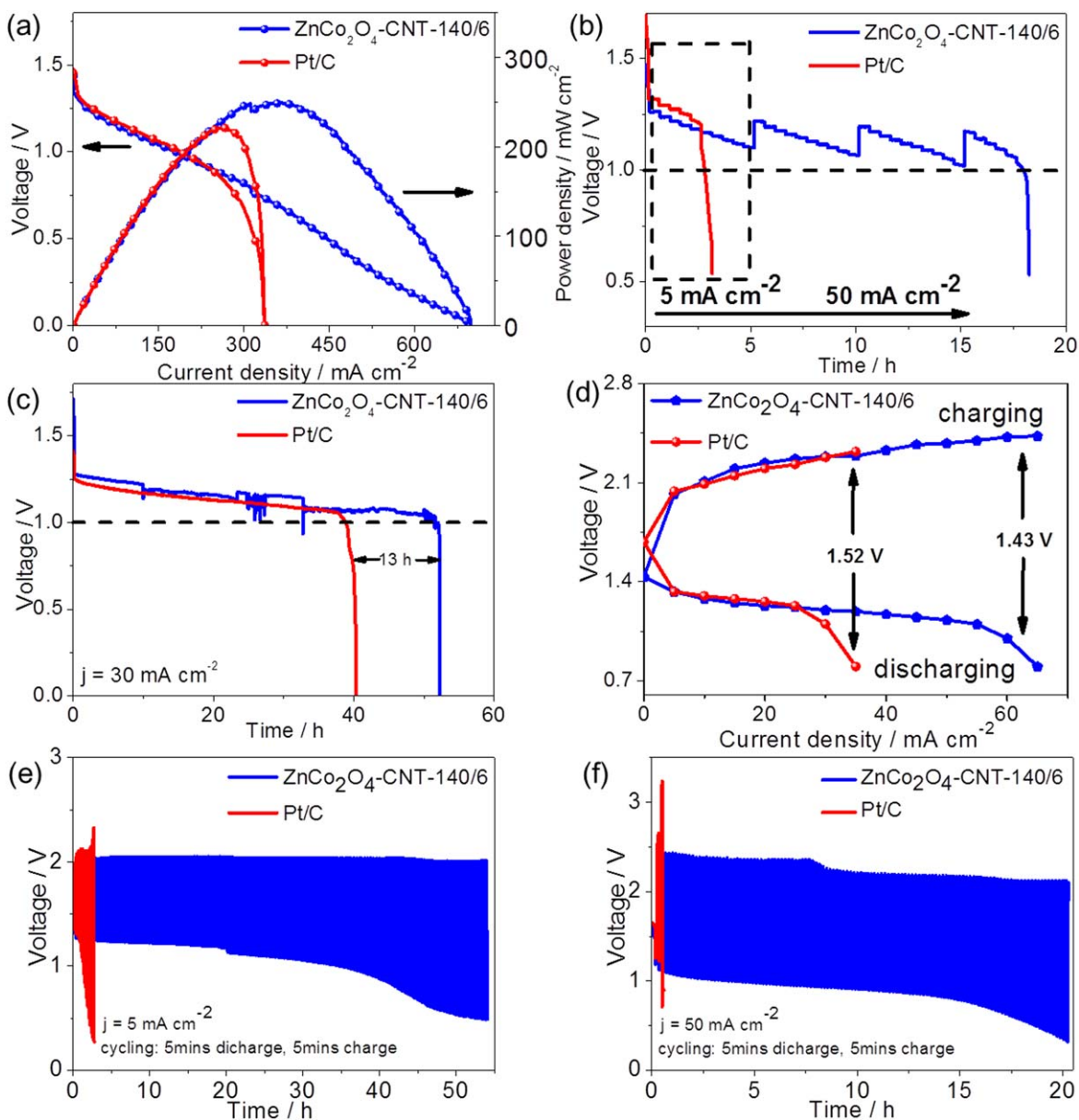
Figure 6. (a) Power density plots of $ZnCo_2O_4$-CNT-140/6 and Pt/C catalysts; (b) The galvanostatic discharge curves of $ZnCo_2O_4$-CNT-140/6 and Pt/C catalysts by using a multi-current step method at several increasing current densities from 5 to 50 mA cm^{-2}; (c) Long time galvanostatic discharge curves of $ZnCo_2O_4$-CNT-140/6 and Pt/C catalysts at a constant current density of 30 mA cm^{-2}; (d) Charge and discharge polarization curves of $ZnCo_2O_4$-CNT-140/6 and Pt/C catalysts by using a multi-current step method at several increasing current densities; (e)–(f) Charge and discharge polarization curves of $ZnCo_2O_4$-CNT-140/6 and Pt/C catalysts under the current densities of 5 mA cm^{-2} and 50 mA cm^{-2}.

$ZnCo_2O_4$-CNT-140/6 catalyst and the Pt/C catalyst increases gradually. The discharge and charge voltage curve of the two catalysts almost coincide at small current density (< 25 mA cm^{-2}). However, the discharge performance of Pt/C catalyst decreased rapidly at a current density over 25 mA cm^{-2}, and the charge-discharge voltage gap is large to 1.52 V at 35 mA cm^{-2}. For $ZnCo_2O_4$-CNT-140/6 catalyst. The charge-discharge voltage gap is 1.43 V at 65 mA cm^{-2}. Meanwhile, the charge and discharge test at 5 mA cm^{-2} and 50 mA cm^{-2} of all catalysts were carried out (Figs. S2a–S2d and Figs. 6e –6f). Figure 6e shows that the voltage of $ZnCo_2O_4$-CNT-140/6 catalyst maintained above 1 V without attenuating lasted for 34.9 h (about 210 cycles) at 5 mA cm^{-2}. In addition, the voltage efficiency of $ZnCo2O4$-CNT-140/6 is 60.3%. While the voltage of Pt/C catalyst maintained above 1 V only lasted for 1.36 h (8 cycles). In order to further expose the charging and discharging performance of the catalyst, a charge-discharge cycling at a large current density of 50 mA cm^{-2} was executed (Fig. 6f). The voltage of

$ZnCo_2O_4$-CNT-140/6 catalyst maintained above 1 V for 4 h (about 24 cycles) at 50 mA cm^{-2}, which better than the Pt/C catalyst (0.43 h). Notably, the voltage drop of charge-discharge maintains no visible change for more than 16 h, further showing the successful application of $ZnCo_2O_4$-CNT-140/6 catalyst in the rechargeable zinc-air battery. These results prove a good ORR/OER performance, and a long-term charge-discharge cycle life of the catalyst.

Wearable electronic devices attract a lot of attention due to its excellent flexibility. Hence, a foldable and flexible zinc-air battery was designed by layer-by-layer method (Fig. 7a). In detail, the bi-metal oxide catalyst spraying on carbon cloth (thinness: 0.36 mm) is used as cathode; Tokuyama A 201 membrane is used as the solid electrolyte, and the 0.03 mm zinc foil was used as the anode. As expected, the two flexible batteries were bent and connected in series to make the small lamp shining (Fig. 7b and Figs. S3a–S3c). Subsequently, Fig. 7c shows the maximal current density and highest power density plot of $ZnCo_2O_4$-CNT-140/6 and Pt/C catalysts after
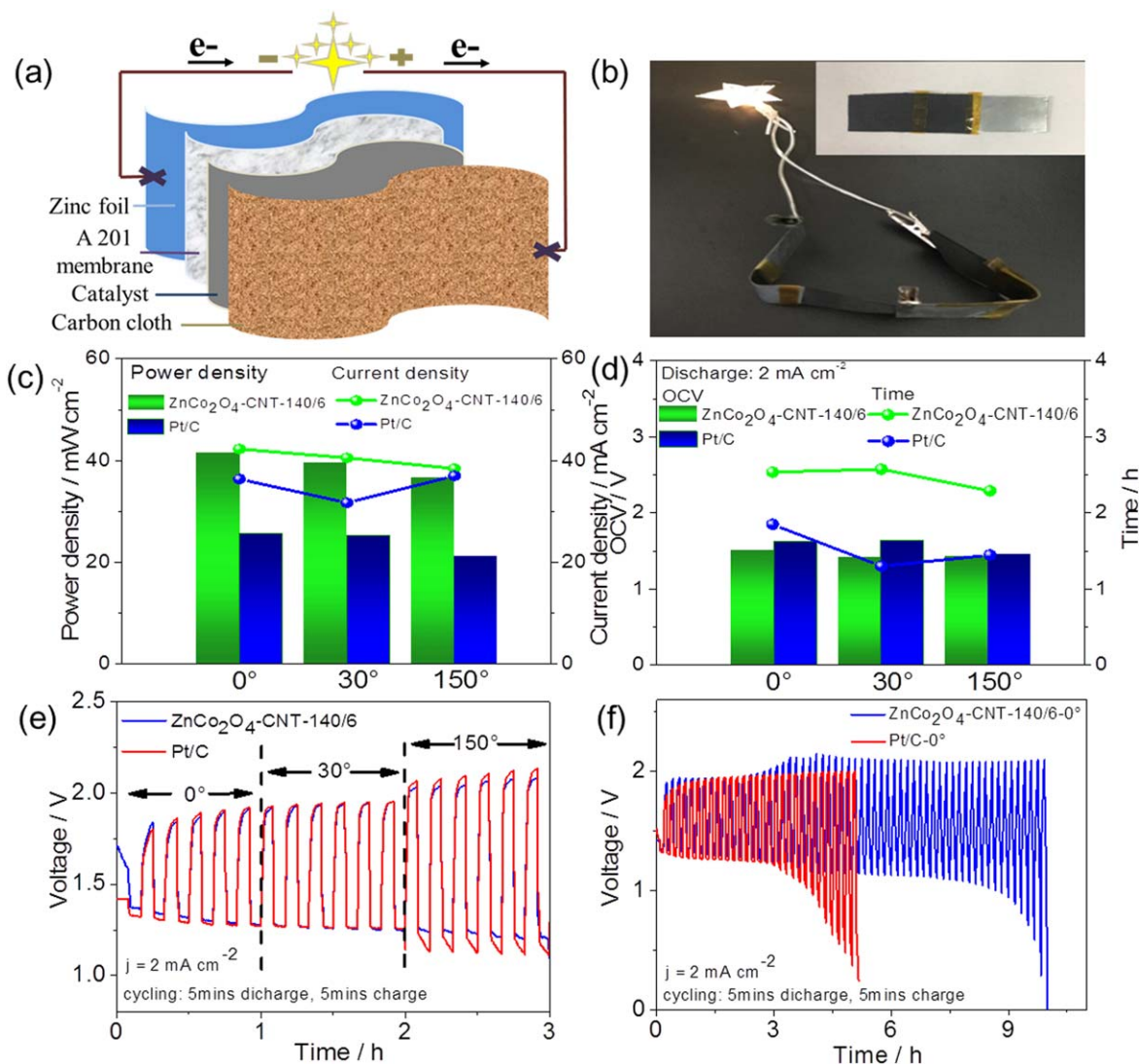
Figure 7. (a) Schematic principle of operation for flexible zinc-air battery; (b) The application of the flexible zinc-air battery; (c) The power density and current density curves of different bending angles of the flexible zinc-air batteries with $ZnCo_2O_4$-CNT-140/6 and Pt/C catalysts; (d) OCV and discharge time curves of different bending angles of the flexible zinc-air batteries with $ZnCo_2O_4$-CNT-140/6 and Pt/C catalysts at a constant discharging current density of 2 mA cm^{-2}; (e) The charge-discharge cycles under different bending angles of the flexible zinc-air batteries with $ZnCo_2O_4$-CNT-140/6 and Pt/C catalysts within the first three hours; (f) Charge-discharge cycles of $ZnCo_2O_4$-CNT-140/6 and Pt/C catalysts under 0° angle.

the batteries were bent to different angles of 0°, 30° and 150°. Notably, the maximum power density of flexible zinc-air batteries with $ZnCo_2O_4$-CNT-140/6 catalyst reach to 41.4 mW cm^{-2}, which is higher than the Pt/C catalyst (25 mW cm^{-2}). The power densities of the hybrid at three angles are basically retained at 40 mW cm^{-2}. The current density of $ZnCo_2O_4$-CNT-140/6 catalyst is always higher than the commercial Pt/C at all angles, which are corresponded to the maximum power density. The details of discharge polarization curves corresponding to power density of three angles can be seen in Figs. S3d–S3f. Obviously, these founds reveal that the flexible batteries have good flexibility. As shown in Fig. 7d, the discharge curves at 0°, 30° and 150° have a similar result at a small current density of 2 mA cm^{-2}. The discharged time of $ZnCo_2O_4$-CNT-140/6 (2.5 h) under the working voltage large 1 V maintains more long than Pt/C (1.3 h). Although the OCV of Pt/C catalyst is always higher than $ZnCo_2O_4$-CNT-140/6 catalyst, the discharge time of $ZnCo_2O_4$-CNT-140/6 catalyst is almost twice longer than noble metal catalyst (Figs. S3g–S3i). Figure 7e shows the charge-discharge cycle curves of flexible batteries at a constant current of 2 mA cm^{-2} under different bending angles. Figure 7e further proves the high flexibility of this type of battery.

$ZnCo_2O_4$-CNT-140/6ill maintained good charge and discharge stability in the process. However, the Pt/C catalyst was significantly attenuated merely after 2 h. Instead, for charge-discharge cycles at 2 mA cm^{-2} (Fig. 7f), the $ZnCo_2O_4$-CNT-140/6 catalyst has a better stability of 9 h (55 cycles) than the Pt/C catalyst (3 h, 18 cycles). These results strongly confirm that $ZnCo_2O_4$-CNT-140/6 catalyst are high active for oxygen reaction and has great potential to replace commercial catalyst.

Conclusions

In summary, we have successfully synthesized a bi-metal spinel oxide hybrid catalyst $ZnCo_2O_4$-CNT with remarkable activity and robust durability of ORR and OER. The results of physical characterization reveal that Zn ions successfully doped into Co_3O_4 at 140 °C for 6 h. In addition, the improved ORR and OER performances is mainly attributed to: i) the strong synergy between $ZnCo_2O_4$ and CNT; ii) the increase of the Co-O bond length; iii) the excellent conductivity and large specific surface area of CNT; and iv) the unique porous flower-shaped structure. As expected, the liquid/flexible rechargeable zinc-air batteries have a high power

density (liquid: 249.4 mW cm^{-2}, flexible: 41.4 mW cm^{-2}), robust dischargeable stability and long-term charge-discharge cycle durability. Notably, the flexible rechargeable zinc-air batteries show remarkable flexibility. The finding gives a new inspiration for improving the catalytic activity of spinel material hybrid materials for wider applications in zinc-air batteries.

Acknowledgments

References

1. S. Pan, J. Ren, X. Fang, and H. Peng, *Adv. Energy Mater.*, **6**, 1501867 (2016).
2. W.-H. Ryu, T.-H. Yoon, S. H. Song, S. Jeon, Y.-J. Park, and I.-D. Kim, *Nano Lett.*, **13**, 4190 (2013).
3. G. Du, X. Liu, Y. Zong, T. S. Hor, A. Yu, and Z. Liu, *Nanoscale*, **5**, 4657 (2013).
4. N. Xu, Y. Cai, L. Peng, J. Qiao, Y. D. Wang, W. M. Chirdon, and X. D. Zhou, *Nanoscale*, **10**, 13626 (2018).
5. Z. Yan, H. Sun, X. Chen, H. Liu, Y. Zhao, H. Li, W. Xie, F. Cheng, and J. Chen, *Nat. Commun.*, **9**, 2373 (2018).
6. R. Cao, J.-S. Lee, M. Liu, and J. Cho, *Adv. Energy Mater.*, **2**, 816 (2012).
7. J. Suntivich, K. J. May, H. A. Gasteiger, J. B. Goodenough, and Y. Shao-Horn, *Science*, **334**, 1383 (2011).
8. N. Xu, X. Li, H. Li, Y. Wei, and J. Qiao, *Sci. Bull.*, **62**, 1216 (2017).
9. G. S. Park, J.-S. Lee, S. T. Kim, S. Park, and J. Cho, *J. Power Sources*, **243**, 267 (2013).
10. Y. Cheng, D. Li, L. Shi, and Z. Xiang, *Nano Energy*, **47**, 361 (2018).
11. Q. Jia, K. Caldwell, J. M. Ziegelbauer, A. Kongkanand, F. T. Wagner, S. Mukerjee, and D. E. Ramaker, *J. Electrochem. Soc.*, **161**, F1323 (2014).
12. Y. He, J. Zhang, G. He, X. Han, X. Zheng, C. Zhong, W. Hu, and Y. Deng, *Nanoscale*, **9**, 8623 (2017).
13. M. Yu, Z. Wang, C. Hou, Z. Wang, C. Liang, C. Zhao, Y. Tong, X. Lu, and S. Yang, *Adv. Mater.*, **29**, 1602868 (2017).
14. X. Li, Y. Fang, X. Lin, M. Tian, X. An, Y. Fu, R. Li, J. Jin, and J. Ma, *J. Mater. Chem. A*, **3**, 17392 (2015).
15. Y. J. Sa, K. Kwon, J. Y. Cheon, F. Kleitz, and S. H. Joo, *J. Mater. Chem. A*, **1**, 9992 (2013).
16. A. Aijaz, J. Masa, C. Rosler, W. Xia, P. Weide, A. J. Botz, R. A. Fischer, W. Schuhmann, and M. Muhler, *Angew. Chem.*, **55**, 4087 (2016).
17. X. T. Wang, T. Ouyang, L. Wang, J. H. Zhong, T. Ma, and Z. Q. Liu, *Angew. Chem.*, **58**, 13291 (2019).
18. Z. Lu et al., *Angew. Chem.*, **58**, 2622 (2019).
19. S. A. Mamuru, K. I. Ozoemena, T. Fukuda, N. Kobayashi, and T. Nyokong, *Electrochim. Acta*, **55**, 6367 (2010).
20. Y.-J. Wang, B. Fang, D. Zhang, A. Li, D. P. Wilkinson, A. Ignaszak, L. Zhang, and J. Zhang, *Electrochem. Energy Rev.*, **1**, 1 (2018).
21. S. Vijayakumar, S.-H. Lee, and K.-S. Ryu, *Electrochim. Acta*, **182**, 979 (2015).
22. T. W. Kim, M. A. Woo, M. Regis, and K.-S. Choi, *J. Phys. Chem. Lett.*, **5**, 2370 (2014).
23. Z. Q. Liu, H. Cheng, N. Li, T. Y. Ma, and Y. Z. Su, *Adv. Mater.*, **28**, 3777 (2016).
24. H. Bordeneuve, S. Guillemet-Fritsch, A. Rousset, S. Schuurman, and V. Poulain, *J. Solid State Chem.*, **182**, 396 (2009).
25. Y.-P. Deng et al., *ACS Energy Lett.*, **2**, 2706 (2017).
26. W. Yan, X. Cao, J. Tian, C. Jin, K. Ke, and R. Yang, *Carbon*, **99**, 195 (2016).
27. W. Yang, S. Yang, J. Guo, G. Sun, and Q. Xin, *Carbon*, **45**, 397 (2007).
28. I. Roche, E. Chainet, M. Chatenet, and J. Vondrak, *J. Phys. Chem. C*, **111**, 1434 (2007).
29. Q. Nie, Y. Cai, N. Xu, L. Peng, and J. Qiao, *ChemElectroChem.*, **5**, 1976 (2018).
30. H. Che, A. Liu, X. Zhang, J. Mu, Y. Bai, and J. Hou, *Ceram. Int.*, **41**, 7556 (2015).
31. S. Xiong, B. Xi, C. Wang, G. Xi, X. Liu, and Y. Qian, *Chem.—Eur. J.*, **13**, 7926 (2007).
32. S. Wang, J. Pu, Y. Tong, Y. Cheng, Y. Gao, and Z. Wang, *J. Mater. Chem. A*, **2**, 5434 (2014).
33. D. Barreca, C. Massignan, S. Daolio, M. Fabrizio, C. Piccirillo, L. Armelao, and E. Tondello, *Chem. Mater.*, **13**, 588 (2001).
34. A. Gulino, G. Fiorito, and I. Fragalà, *J. Mater. Chem.*, **13**, 861 (2003).
35. W. Wei, W. Chen, and D. G. Ivey, *Chem. Mater.*, **20**, 1941 (2008).
36. J. F. Marco, J. R. Gancedo, M. Gracia, J. L. Gautier, E. Ríos, and F. J. Berry, *J. Solid State Chem.*, **153**, 74 (2000).
37. Y. E. Roginskaya, O. V. Morozova, E. N. Lubnin, Y. E. Ulitina, G. V. Lopukhova, and S. Trasatti, *Langmuir*, **13**, 4621 (1997).
38. J. Li, J. Wang, D. Wexler, D. Shi, J. Liang, H. Liu, S. Xiong, and Y. Qian, *J. Mater. Chem. A*, **1**, 15292 (2013).
39. S. G. Mohamed et al., *RSC Adv.*, **3**, 20143 (2013).
40. N. Xu, Y. Zhang, T. Zhang, Y. Liu, and J. Qiao, *Nano Energy*, **57**, 176 (2019).
41. N. Xu, Y. Zhang, M. Wang, X. Fan, T. Zhang, L. Peng, X.-D. Zhou, and J. Qiao, *Nano Energy*, **65**, 104021 (2019).
42. X. Liu, Z. Chang, L. Luo, T. Xu, X. Lei, J. Liu, and X. Sun, *Chem. Mater.*, **26**, 1889 (2014).
43. H. Wang et al., *Int. J. Hydrogen Energy*, **41**, 13024 (2016).